ACS APPLIED MATERIALS & INTERFACES

Research Article

www.acsami.org

Air-Stable Efficient Inverted Polymer Solar Cells Using Solution-Processed Nanocrystalline ZnO Interfacial Layer

Mein Jin Tan,[†] Shu Zhong,[‡] Jun Li,[†] Zhikuan Chen,*[,†] and Wei Chen*[,‡,§]

[†]Institute of Materials Research and Engineering, A*STAR Singapore, 3 Research Link, Singapore 117602

[‡]Department of Chemistry, National University of Singapore, 3 Science Drive 2, Singapore 117543

[§]Department of Physics, National University of Singapore, 2 Science Drive 3, Singapore 117542

ABSTRACT: In this work, efficient bulk heterojunction (BHJ) organic solar cells (OSC) in inverted configuration have been demonstrated. Power conversion efficiency (PCE) of 3.7% is reported for OSC employing silver top electrodes, molybdenum trioxide (MoO_3) as the hole-transport interlayer (HTL), active layer comprising of poly-3-hexylthiophene (P3HT) and [6,6]-phenyl C_{61} butyric acid methyl ester (PCBM) as well as a nanocrystalline solution-synthesized zinc oxide (ZnO) nanoparticle (NP) film as the electron-transport layer (ETL). By using solution-processable ZnO crystalline NPs as ETL, we can eliminate the typical high temperature processing/annealing step, which is widely adopted in the conventional ZnO ETL fabrication process via the sol−gel method. Such highly crystalline ZnO NP films can enhance charge collection at the electrodes. It is also found that inverted OSCs exhibit greater air stability and lifetime performance compared to the OSC employing the normal structure.

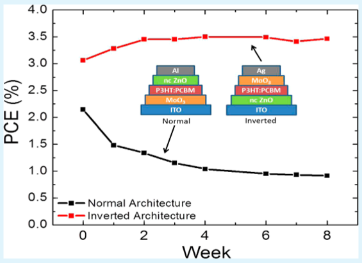

KEYWORDS: *zinc oxide, inverted polymer solar cells, lifetime stability, electron transport layer, P3HT, solution processable*

1. INTRODUCTION

Organic solar cells (OSCs) have attracted much interest in recent years due to their advantage over traditional silicon-based solar cells, such as roll-to-roll production as well as the ability to be fabricated on flexible substrates and in large areas.[1,2] However, the main drawback for OSCs is its low power conversion efficiency (PCE) of around 10% as compared to silicon-based cells of around 20%.[3,4] Several factors such as large exciton binding energies, short exciton diffusion lengths, relatively lower charge mobilities, and poorer charge collection at the electrodes have been identified as roadblocks to more efficient OSC devices.[3−5] The introduction of the bulk heterojunction (BHJ) architecture has circumvented the problem of short exciton diffusion lengths. Novel polymeric materials with higher charge mobilities have also been developed. To improve charge carrier collection, interfacial materials (between metal/organic and metal oxide/organic interfaces) are necessary to provide favorable energy level alignment as well as matching morphological traits.

OSCs suffer from poor device stability and shorter lifetime due to the use of a low work-function (WF) metal electrode such as aluminum at the top of the device. For the "normal" device architecture where electrons are extracted via the top metal electrode and holes via the bottom transparent electrode, usually indium-doped tin oxide (ITO), the OSCs degrade quickly upon exposure to ambient conditions and allow oxygen and water to enter into the active layer of the device, which can further degrade performance.[6−9] Device stability can be improved by using an inverted device architecture, where a high WF metal electrode with greater ambient stability such as silver or gold is used, and the holes are extracted via the top metal electrode instead. However, the bottom transparent electrode usually consists of high WF ITO, making electron collection a big challenge in the inverted architecture. Therefore, it is crucial to develop suitable interfacial materials to ensure efficient charge carrier collection and extraction at the respective electrodes.[10]

In this work, the inverted architecture is adopted and zinc oxide (ZnO) is used as the electron transport layer (ETL) to be coated on ITO to facilitate electron collection. Metal oxides have been used in both inverted and normal OSC architectures, such as TiO_2 and ZnO for cathode interface and NiO, MoO_3, and WO_3 for the anode interface.[7,11−15] However, some of these layers are obtained via sol−gel methods, which provide an amorphous layer under mild annealing conditions. These layers function more as an energy alignment interlayer and optical spacer.[7] ZnO is chosen for its high conductivity, wide band gap, and ease of synthesis to obtain size controllable crystalline nanoparticles, accounting for its numerous applications in organic electronics.[16−19] The active layer comprises poly-3-hexyl-thiophene (P3HT) and [6,6]-phenyl-C_{61}-butyric acid methyl ester (PCBM), which is currently the most referred benchmark for OSCs. MoO_3 is chosen as the hole transport layer (HTL) due to its favorable energy level alignment with the HOMO level of P3HT. There have been reports using the same material components,[20−23] but the PCE of 3.7% obtained in this work is the highest thus far. Moreover, the use of such crystalline ZnO NP interfacial layer can avoid the high

Received: December 6, 2012
Accepted: May 1, 2013
Published: May 6, 2013

dx.doi.org/10.1021/am303004r | *ACS Appl. Mater. Interfaces* 2013, 5, 4696−4701

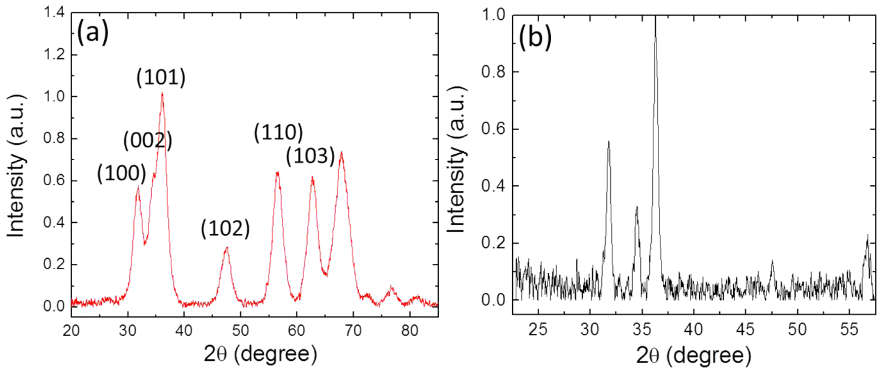

Figure 1. XRD spectra of (a) ZnO nanoparticle powder and (b) ZnO film on SiO_2 substrate.

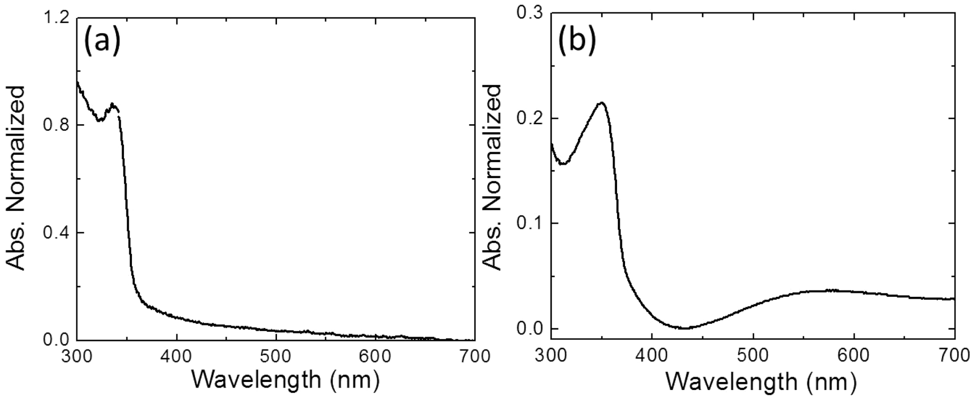

Figure 2. UV−vis spectra of (a) ZnO nanoparticle solution and (b) ZnO film on glass/ITO substrate.

temperature post annealing process widely adopted for the sol−gel derived ZnO interfacial layer, hence to bypass the ETL electrode damaging issue during this annealing step.[24]

2. EXPERIMENTAL SECTION

Zinc acetate dihydrate (ZnAc) (98−101%) and potassium hydroxide (KOH) (85%) were purchased from Alfa Aesar and Merck, respectively, and used as received. P3HT and PCBM were purchased from Rieke Metals and Nano-C, respectively, and were used as received.

2.1. Synthesis of Crystalline ZnO Nanoparticles. Synthesis of crystalline ZnO nanoparticles was adopted from Meulenkamp.[25] Briefly, 3 mmol of ZnAc was first dissolved in 30 mL of ethanol under heating at 70 °C. Once all of the ZnAc was fully dissolved, heating was stopped to cool the solution. A total of 5.1 mmol of KOH was added into 30 mL of ethanol and dissolved by sonication. Both solutions were then cooled to 0 °C. The KOH−ethanol solution was added drop by drop into the ZnAc−ethanol solution. The resultant solution was stored in a 4 °C fridge for 12 h to reach full precipitation. Extraction of the ZnO nanoparticles was also adopted from the method introduced by Meulenkamp.[25] A nonpolar organic solvent such as hexane or heptane was used to precipitate ZnO nanoparticles out of the solution and extracted via centrifugation. The extracted particles were dried in air for 8 h before being redispersed in ethanol for future use. Prior to the device fabrication, the ZnO nanoparticle solution was filtered to obtain a clear colorless solution that remained stable for up to 1 month.

2.2. Device Fabrication. ITO coated glass substrates were first sonicated and cleaned in acetone and 2-propanol. ZnO NP solution was spin-coated at 500 rpm for 90 s onto the ITO substrates to obtain a thickness of 20 nm and heated at 120 °C for 10 min to remove excess solvent and moisture. The substrates were then moved to a nitrogen-filled glovebox where the active layer consisting of P3HT:PCBM (1:0.8 weight ratio) dissolved in 1,2-dichlorobenzene (2% , w/v) was spin-coated at 500 rpm for 120 s onto the ZnO NP treated ITO substrates to obtain a thickness of 180 nm. The coated substrates were preannealed at 120 °C for 10 min to improve crystallinity of P3HT[26] before being moved to a thermal evaporator where molybdenum trioxide (MoO_3) (5 nm) and silver electrodes (100 nm) were evaporated to complete the device.

2.3. Characterization. Current−voltage (J−V) measurements were done under AM1.5 conditions with a SanEi solar simulator and recorded by a Keithley 2400 source-meter. Film thicknesses were measured by Tencor 10 surface profiler. X-ray diffraction (XRD) spectrum was obtained by a Phillips GADDS. UV−vis absorption and transmittance were measured using a Shimadzu Spectrometer.

In situ ultraviolet photoemission spectroscopy (UPS) experiments were performed in a custom designed ultrahigh vacuum (UHV) system with He 1α (21.2 eV) as the excitation source. All UPS spectra were recorded with Omicron EA 125 hemispherical analyzer at normal emission angle at room temperature (RT). Vacuum level shifts were measured from the linear extrapolation of the cutoff of the low kinetic energy part of UPS spectra with a −5 V sample bias. The sample work function ϕ was obtained through the equation $\phi = h\nu - W$, where W is the spectrum width (the energy difference between the substrate Fermi level and low kinetic energy onset). The binding energy of all UPS spectra were calibrated and referenced to the Fermi level of a sputter-cleaned silver sample. Vacuum-sublimation purified PCBM was thermally evaporated onto the ZnO NP layer covered ITO substrates at RT from a commercial Knudsen cell in the growth chamber. Deposition rate of $\sim$0.15 nm/min at 245 °C was precalibrated by a quartz-crystal-microbalance (QCM). The nominal thickness of PCBM was also estimated from the attenuation of the Si 2p peak intensity from the SiO_2 substrate before and after deposition.

3. RESULTS AND DISCUSSION

3.1. Characterization of ZnO NP and Film. As shown in the XRD spectrum (Figure 1a), the extracted ZnO NPs are crystalline and exhibit the wurzite structure. The broad peaks observed in the spectra indicate the small particle size of the ZnO synthesized. Figure 1b shows the XRD spectrum for a film sample and clearly reveals the wurzite structure of bulk ZnO. The direct use of such crystalline ZnO nanoparticle film as the ITO electrode interfacial layer can eliminate the need for high temperature post-annealing to transform ZnO layer to a crystalline layer. Moreover, this can significantly simplify the device fabrication process and avoid possible damages to the ITO electrodes during the high temperature annealing process.[24] A crystalline layer not only provides optimal energy level alignment but also better conductivity for more efficient charge transport and extraction.

Figure 2a shows a UV−vis spectrum of ZnO NPs in solution, and an excitonic shoulder peak at around 345 nm is observed. Bulk ZnO is known to have a peak of around 365 nm. This blue shift in spectrum can be attributed to the quantum confinement effect,[15] thus confirming the small particle size observed in the XRD spectra. Figure 2b shows a UV−vis spectrum of a ZnO film coated on an ITO substrate, and both are congruent.

For an effective interlayer, it should not absorb within visible light range to allow maximum amount of light to pass through the active organic layer. Figure 3 displays the UV−vis transmittance spectra of a ZnO NP film, where outstanding transmission of visible light is exhibited (>95%). As such, the ZnO NP film serves as an excellent optically transparent interlayer in the visible light range. It should also be noted in Figure 3 that the transmittance goes above 100%. This can be explained by Fresnel's Reflection in Multilayer Structures,[27] where a material of refractive index in between that of the substrate and air can result in reduced reflective effects and a higher percentage of light passing through the multilayer structure as compared to the substrate alone. This is also the basis of antireflection applications using ZnO.[28]

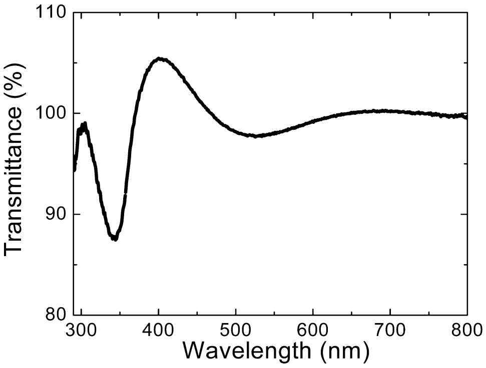

Figure 3. UV−vis transmittance spectra of a 20 nm ZnO NP film coated on ITO glass.

Scanning electron microscopy (SEM) and atomic force microscopy (AFM) measurements were performed on ZnO NP film samples to further understand the morphology. The SEM picture displayed in Figure 4a shows a dense but nanoporous ZnO NP film. This indicates that the spin-coating method provided excellent coverage of ZnO NP over the entire ITO−glass substrate. The AFM picture shown in Figure 4b exhibited the nanoparticle nature of the ZnO NP film and the roughness was estimated to be around 5 nm.

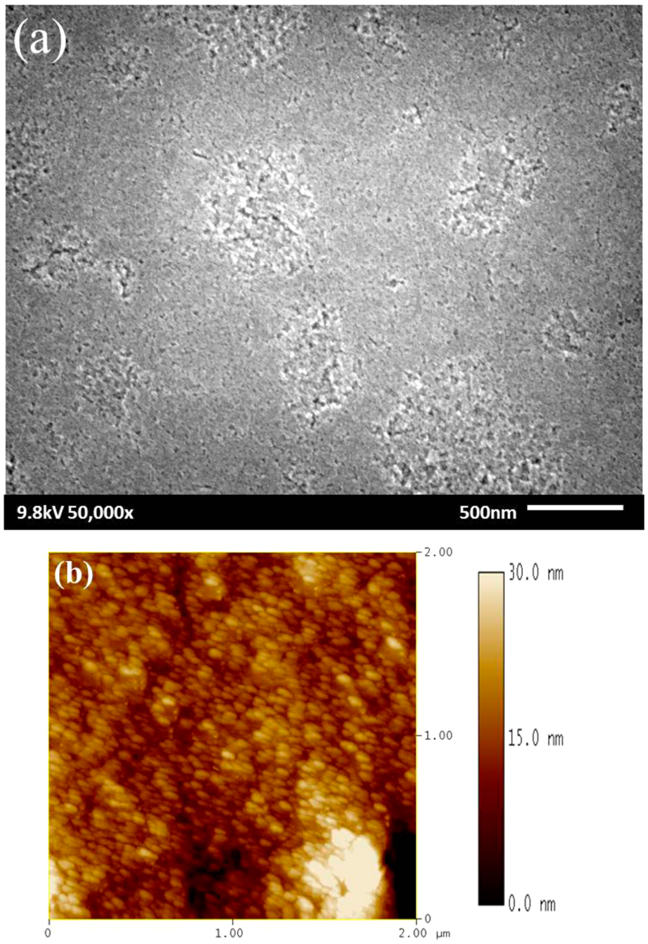

Figure 4. (a) SEM micrograph and (b) AFM picture of a 20 nm ZnO NP film coated on glass/ITO substrate.

In order to evaluate the energy level alignment of ZnO NP interlayer with n-type organic material, in situ UPS measurements were carried out. In our experiment, $PC_{60}BM$ was chosen as the model n-type material. Figure 5 shows the evolution of the thickness-dependent UPS spectra for $PC_{60}BM$ on ZnO NP film at the low kinetic energy region (Figure 5a), the valence band region (Figure 5b), and the low binding energy region near the Fermi level (Figure 5c) during the deposition of $PC_{60}BM$ on ZnO NP film. The bottom spectra in Figure 5a−c correspond to the pristine ZnO NP film on ITO. The work function was measured to be 3.81 eV. After the sequential deposition of 10 nm PCBM film on the ZnO NP layer, a slight upward vacuum level shift of about 0.17 eV was observed. At the same time, the HOMO leading edge of $PC_{60}BM$ marked by the solid line in Figure 5c was located at 1.88 eV below the Fermi level. Figure 5d shows the energy level diagram at the PCBM/ZnO NP film interface. The HOMO position of the PCBM was derived from the UPS measurements. The transport band gap and hence the LUMO positions were taken from previously reported inverse photoemission spectroscopy (IPES) measurements.[29] Clearly, the LUMO of the PCBM was very close to the Fermi level (about 0.22 eV above the Fermi level), thus minimizing the energy barrier for electron charge transfer between PCBM and ZnO. Therefore ZnO NP film can be used as an efficient interfacial layer for electron extraction and transport.

3.2. Device Characterization. The crystalline ZnO NP layer was incorporated into an inverted architecture BHJ OSC with the active blend layer of P3HT and PCBM. MoO_3 was used as a hole-collecting layer and topped by a silver electrode.

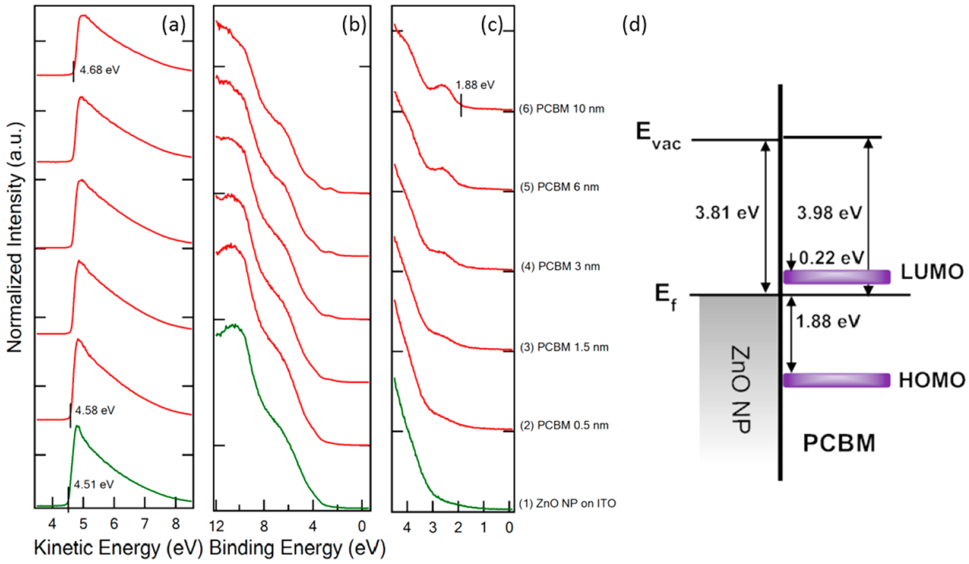

Figure 5. UPS spectra at (a) the low kinetic energy region (secondary electron cutoff), (b) valence band region, and (c) the low binding energy region near the Fermi level during the deposition of PCBM on ZnO NP covered ITO substrate. (d) Schematic energy level diagrams of PCBM on ZnO NP film.

The best power conversion efficiency (PCE) obtained was 3.7% (Figure 6 and Table 1), which is the highest reported so far for the OSC system comprising of the above-mentioned materials[30,31] and is comparable to that achieved by the normal architecture as reported elsewhere.[32] The good performance can be attributed to the factors characterized above, that is, crystalline ZnO NPs were used to confer higher conductivity and high transmittance in the visible light range as well as excellent energy level matching between ZnO NP film and PCBM. Furthermore, for the control device without the ZnO ETL (i.e., P3HT:PCBM directly contacting the ITO electrode), the V_{oc} was drastically reduced and the S-curve was typically observed in the device, indicating poor charge collection. This highlights the importance of the ETL in providing appropriate energy level alignment to achieve proper “inversion” of the device.[33−35]

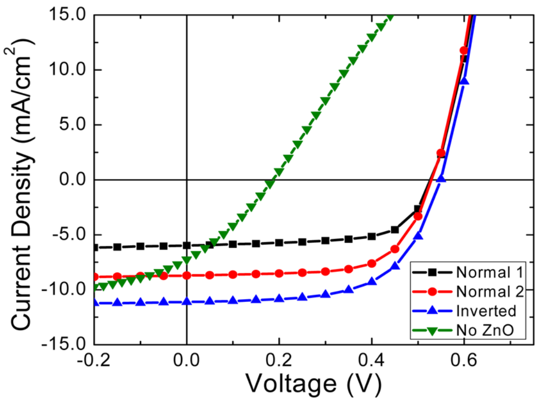

Figure 6. *J*−*V* characteristics and device data for different device architecture.

Table 1. *J*−*V* Statistical Data for Inverted and Normal Device Architecture

sample	V_{oc}, V	J_{sc}, mA cm^{-2}	FF, %	PCE, %
Normal 1	0.52	6.0	66.3	2.07
Normal 2	0.53	8.7	66	3.04
Inverted	0.55	11.0	61.5	3.72
no ZnO	0.18	7.23	31.5	0.41

Lifetime studies were also carried out to compare the stability of the top metal electrode used. A normal architecture OSC was fabricated using the same materials with aluminum as the top electrode and the order of the materials flipped (Figure 7, Normal 1). The devices were not encapsulated and left in ambient condition and were only brought into a nitrogen environment (glovebox) for *J*−*V* measurements. As shown in Figure 8, the lifetime of the inverted structure out-performed that of the normal structure (Table 2 shows the *J*−*V* device characteristics). This corroborates previous reports that the inverted structure is indeed more robust and stable due to the usage of a higher WF top metal electrode.[3] Moreover, the performance of the inverted OSC steadily improved until it reached a maximum (typically 3 days later); whereas that of the normal structure dropped almost immediately after fabrication. This is attributed to the slight increase in the WF of silver as it is slowly oxidized by ambient atmosphere resulting in a more favorable energy level alignment for holes extraction.[36,37] Another advantage of using silver as top electrode is the compatibility with high throughput roll-to-roll printing techniques as silver can be printed, doing away with the use of costly high vacuum thermal evaporation methods.[38]

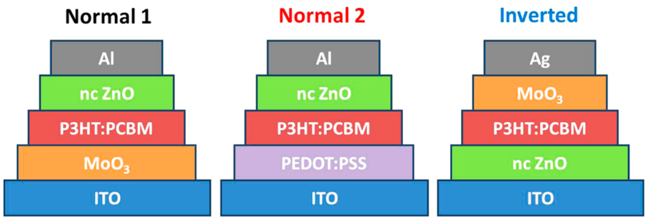

Figure 7. Device architecture illustration for the two normal OPVs using MoO_3 or PEDOT:PSS as anode interfacial layers and inverted OPV with nanocrystalline ZnO (nc ZnO) as cathode interfacial layer.

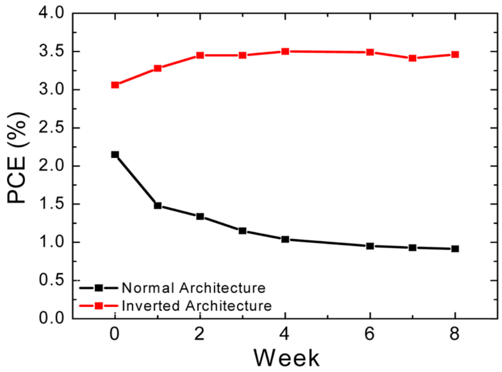

Figure 8. Lifetime studies of Normal and Inverted architecture devices.

Table 2. *J*−*V* Statistical Lifetime Data for Inverted and Normal Device Architecture

sample	V_{oc}, V	J_{sc}, mA cm^{-2}	FF, %	PCE, %
Initial				
Normal	0.53	6.33	65.5	2.19
Inverted	0.57	10.18	52.5	3.05
After 8 weeks				
Normal	0.47	3.41	57.5	0.92
Inverted	0.58	9.93	61.2	3.52

4. CONCLUSION

A high PCE of 3.7% for an inverted OSC architecture using P3HT:PCBM was demonstrated in this work, which is the highest reported PCE so far for the materials used in this OSC system. A solution-processed crystalline ZnO layer was directly used as an ITO electrode interfacial layer, omitting the need for a high temperature post-annealing process widely adopted for the conventional sol−gel derived ZnO interfacial layer. The optimal energy level alignment to PCBM and high conductivity provided by the crystalline ZnO layer resulted in more efficient charge transport and extraction, leading to the good PCE performance. The inverted architecture exhibited greater ambient stability as compared to the normal structure. This provides a good basis and platform for implementing the inverted structure system to other low-bandgap materials that give better performance than P3HT, leading to the development of OSCs with better efficiency and longer lifetime.

■ AUTHOR INFORMATION

Corresponding Authors

*E-mail: zk-chen@imre.a-star.edu.sg (Z.C.), phycw@nus.edu.sg (W.C.).

Notes

The authors declare no competing financial interest.

■ ACKNOWLEDGMENTS

M.J.T. would like to thank Dr. Dongchen Qi for advice on UPS data analysis and Mr. Jianqiang Zhong for valuable feedback. The authors acknowledge the financial support from MOE Grants R143-000-505-112, R143-000-530-112, and R143-000-542-112 and NUS YIA Grant R143-000-452-101.

■ REFERENCES

(1) Brabec, C. J.; Sariciftci, N. S.; Hummelen, J. C. *Adv. Funct. Mater.* **2011**, *11*, 15−26.

(2) Yu, G.; Gao, J.; Hummelen, J. C.; Wudl, F.; Heeger, A. J. *Science* **1995**, *270*, 1789−1791.

(3) Zhang, F. J.; Xu, X. W.; Tang, W. H.; Zhang, J.; Zhuo, Z. L.; Wang, J.; Wang, J.; Xu, Z.; Wang, Y. S. *Sol. Energy Mater. Sol. Cells* **2011**, *95*, 1785−1799.

(4) He, Z. C.; Zhong, C. M.; Su, S. J.; Xu, M.; Wu, H. B.; Cao, Y. *Nat. Photonics* **2012**, *6*, 591−595.

(5) Cai, W. Z.; Gong, X.; Cao, Y. *Sol. Energy Mater. Sol. Cells* **2010**, *94*, 114−127.

(6) Zou, J. Y.; Yip, H. L.; Zhang, Y.; Gao, Y.; Chien, S. C.; O'Malley, K.; Chueh, C. C.; Chen, H. Z.; Jen, A. K. Y. *Adv. Funct. Mater.* **2012**, *22*, 2804−2811.

(7) Sun, Y. M.; Seo, J. H.; Takacs, C. J.; Seifter, J.; Heeger, A. J. *Adv. Mater.* **2011**, *23*, 1679−1683.

(8) You, J. B.; Chen, C. C.; Dou, L. T.; Murase, S.; Duan, H. S.; Hawks, S. A.; Xu, T.; Son, H. J.; Yu, L. P.; Li, G.; Yang, Y. *Adv. Mater.* **2012**, *24*, 5267−5272.

(9) Jorgensen, M.; Norrman, K.; Krebs, F. C. *Sol. Energy Mater. Sol. Cells* **2008**, *92*, 686−714.

(10) Zhu, Y. X.; Xu, X. F.; Zhang, L. J.; Chen, J. W.; Cao, Y. *Sol. Energy Mater. Sol. Cells* **2010**, *97*, 83−88.

(11) Ratcliff, E. L.; Zacher, B.; Armstrong, N. R. *J. Phys. Chem. Lett.* **2011**, *2*, 1337−1350.

(12) Yang, T. B.; Cai, W. Z.; Qin, D. H.; Wang, E. G.; Lan, L. F.; Gong, X.; Peng, J. B.; Cao, Y. *J. Phys. Chem. C* **2010**, *114*, 6849−6853.

(13) Hau, S. K.; Yip, H.; Baek, N. S.; Zou, J.; O'Malley, K.; Jen, A. K. Y. *Appl. Phys. Lett.* **2008**, *92*, 253301.

(14) Hau, S. K.; Yip, H.; Ma, H.; Jen, A. K. Y. *Appl. Phys. Lett.* **2008**, *93*, 233304.

(15) Oh, H.; Krantz, J.; Litzov, I.; Stubhan, T.; Pinna, L.; Brabec, C. J. *Sol. Energy Mater. Sol. Cells* **2011**, *95*, 2194−2199.

(16) Hau, S. K.; Yip, H.; Orcton, O.; Baek, N. S.; Jen, A. K. Y. *J. Mater. Chem.* **2008**, *18*, 5113−5119.

(17) Kim, J. Y.; Kim, S. H.; Lee, H. H.; Lee, K.; Ma, W.; Gong, X.; Heeger, A. J. *Adv. Mater.* **2006**, *18*, 572−576.

(18) Beek, W. J. E.; Wienk, M. M.; Janssen, R. A. J. *Adv. Mater.* **2004**, *16*, 1009−1013.

(19) Baeten, L.; Conings, B.; Boyen, H.; D'Haen, J.; Hardy, A.; D'Olieslaeger, M.; Manca, J. V.; Van Bael, M. K. *Adv. Mater.* **2011**, *23*, 2802−2805.

(20) Monson, T. C.; Lloyd, M. T.; Olson, D. C.; Lee, Y.; Hsu, J. W. P. *Adv. Mater.* **2008**, *20*, 4755−4759.

(21) Zhang, B.; Lee, D.; Chae, H.; Park, C.; Cho, S. M. *Korean J. Chem. Eng.* **2010**, *27*, 999−1002.

(22) Song, P.; Qin, W.; Ding, G.; Yan, Q.; Yang, L.; Yin, S. *Optoelectron. Lett.* **2011**, *7*, 330−333.

(23) Yang, T.; Qin, D.; Lan, L.; Huang, W.; Gong, X.; Peng, J.; Cao, Y. *Sci. China Chem.* **2012**, *55*, 755−759.

(24) Kim, Y.; Shin, S.; Song, J.; Cho, D.; Lee, H.; Jung, Y. *J. Mater. Res.* **2005**, *20*, 1574−1579.

(25) Meulenkanp, E. A. *J. Phys. Chem. B* **1998**, *102*, 5566−5572.

(26) Ruderer, M. A.; Guo, S.; Meier, R.; Chiang, H.; Korstgens, V.; Wiedersich, J.; Perlich, J.; Roth, S. V.; Muller-Buschbaum, P. *Adv. Funct. Mater.* **2011**, *21*, 3382−3391.

(27) Harbecke, B. *Appl. Phys. B: Laser Opt.* **1986**, *39*, 165−170.

(28) Salman, K. A.; Hassan, K. O. Z. *Solar Energy* **2012**, *86*, 541−547.

(29) Akaike, K.; Kanai, K.; Yoshida, H.; Tsutsumi, J. Y.; Nishi, T.; Sato, N.; Ouchi, Y.; Seki, K. *J. Appl. Phys.* **2008**, *104*, 023710.

(30) White, M. S.; Olson, D. C.; Shaheen, S. E.; Kopidakis, N.; Ginley, D. S. *Appl. Phys. Lett.* **2006**, *89*, 143517.

(31) Kyaw, A. K. K.; Sun, X. W.; Jiang, C. Y.; Lo, G. Q.; Zhao, D. W.; Kwong, D. L. *Appl. Phys. Lett.* **2008**, *93*, 221107.

(32) Dang, M. T.; Hirsch, L.; Wantz, G. *Adv. Mater.* **2011**, *23*, 3597−3602.

(33) Liang, Z.; Zhang, Q.; Wiranwetchayan, O.; Xi, J.; Yang, Z.; Park, K.; Li, C.; Cao, G. *Adv. Funct. Mater.* **2012**, *22*, 2194−2201.

(34) Ma, Z.; Tang, Z.; Wang, E.; Andersson, M. R.; Inganas, O.; Zhang, F. *J. Phys. Chem. C* **2012**, *116*, 24462−24468.

(35) Lim, D. C.; Shim, W. H.; Kim, K.; Seo, H. O.; Lim, J.; Jeong, Y.; Kim, Y. D.; Lee, K. H. *Sol. Energy Mater. Sol. Cells* **2011**, *95*, 3036–3040.

(36) Chu, C. W.; Shrotriya, V.; Li, G.; Yang, Y. *Appl. Phy. Lett.* **2006**, *88*, 153504.

(37) Xu, Z.; Chen, L. M.; Yang, G. W.; Huang, C. H.; Hou, J. H.; Wu, Y.; Li, G.; Hsu, C. S.; Yang, Y. *Adv. Funct. Mater.* **2009**, *19*, 1227–1234.

(38) Krebs, F. C.; Fyenbo, J.; Jorgensen, M. *J. Mater. Chem.* **2010**, *20*, 8994–9001.